Progress In Electromagnetics Research C, Vol. 137, 39–51, 2023

Low Profile Wideband Polarization Rotation Reflective Metasurface

**Karamkulambel K. Indhu[1, *], Abhilash Achariparambil[1], Paulbert Thomas[3],
Ramakrishnan A. Kumar[1], Deepti D. Krishna[1], and Aanandan Chandroth[2]**

Abstract—A low profile metasurface, which rotates the polarisation of incident electromagnetic wave upon reflection, is presented in this study. The design, which works over a large bandwidth of 67%, is achieved by combining the effect of a circle and a triangle forming a unit cell. By proper modification, the array is found to be useful in RCS reduction over a broad frequency range. Unlike many earlier designs, this structure is of single layer and can be fabricated using standard process on a thin substrate which is inexpensive and easily available. The results are presented with simulation and experiment.

1. INTRODUCTION

Electromagnetic wave polarisation characterizes orientation of electric field carried by such waves. Since many exciting phenomena are sensitive to polarisation, it is desirable to effectively manage and modify the polarisation state of electromagnetic waves generally. The polarisation convertor rotates the polarisation of an incident wave in orthogonal direction. Polarization rotation reflective surface (PRRS) that combines reflection and polarisation rotation finds widespread utilizations like the design of reflector antennas [1, 2], the reduction of RCS, etc. [3–9]. The literature cites several instances of PRRS, including a double V-shaped metasurface that offers 77% polarisation rotation bandwidth with 90% polarization conversion ratio (PCR) [10]. A cross-polarization converter based on an anisotropic metasurface with a polarization rotator (PR) bandwidth of 59.2% and a PCR of 99% is reported [11]. Recently, a two-layered anisotropic surface with PCR more than 90% allows a broader bandwidth of 121% [12]. A broad band (86%) hollow rhombus-shaped surface with PCR greater than 90% is also reported in [13]. Several researchers have reported the development of polarization manipulation surfaces for diverse applications, at infrared radiation (IR) and Terahertz range [14–19].

Polarization rotation reflective surface (PRRS) is extensively used for radar cross-section (RCS) reduction [3–9]. Other types of structures such as artificial magnetic conductors (AMCs) [20–22], electromagnetic bandgap (EBG) [23], and frequency selective surfaces (FSSs) [24]. Broadband RCS reduction is obtained by combining AMC/EBG/FSS unit cells or by combining AMC/EBG/FSS surfaces having distinct resonances. Two-layer chessboard arrangement [22] yields even greater bandwidths. In [23], dual-band EBG structures are used to achieve a 10 dB RCS reduction.

Unlike the above-mentioned methods, RCS reductions can be achieved by putting PRRS in a checkerboard arrangement with orthogonal orientation. It reduces manufacturing difficulties and costs by streamlining the design. Due to this important property, there has been increased interest in PRRS-related RCS reduction usages such as target structure RCS-reduction [3–7] and antenna RCS-reduction [8, 9]. An ultra-wideband PRRS having a larger bandwidth of 103.6% and PCR being more than 50% using quasi-L shaped patch giving 10 dB RCS reduction is reported [3]. Another PRRS made up of L- and square-shaped patches along with four vias gave −10 dB RCS reduction bandwidth of

---

Received 5 May 2023, Accepted 9 August 2023, Scheduled 28 August 2023

* Corresponding author: Karamkulambel Kunjappan Indhu (indhukk@cusat.ac.in).

[1] Department of Electronics, Cochin University of Science and Technology, India. [2] ACARR, Cochin University of Science and Technology, India. [3] Department of Electronics, The Cochin College, Kochi, India.

98% [4]. Further proposal for a broadband architecture is proposed in [5] by a polarization conversion metasurface with PCR over 90% whose 10 dB radar cross section bandwidth is 62%. In [6], a PRRS with PCR of 99% was developed with a 10 dB RCS reduction bandwidth of 97.6% by employing four vias. The polarisation conversion metasurface formed by five differently-sized square patches arranged in a line along a 45-degree diagonal direction is also reported [7]. This design resulted in a 5 dB reduction in RCS within a bandwidth ranging from 3.7 to 15.9 GHz. Though aforementioned structures have attained wideband behaviours, their inefficiency stems from the fact that the bandwidth enhancement comes at the expense of its excessively large size or increased design complexity. Therefore, for practical purposes, thin low-profile structures with larger bandwidth and higher PCR are needed.

In this paper, a low profile wideband PRRS with high PCR is presented. Expanding the PR bandwidth, boosting PCR, and reducing the thickness and size of the unit cell are the objectives of the design process that result in creating this structure. The PCR of the structure is more than 90%, and its unit cell dimensions are $0.240\lambda_0 \times 0.240\lambda_0 \times 0.060\lambda_0$ giving a PR bandwidth of 67%. In addition to these primary benefits, this structure is lightweight with low cost, which contribute to its practical efficiency. The unit cells are arranged on a layout similar to a chessboard, with orthogonal orientation in each of the four parts in order to lower the RCS across a broader bandwidth also demonstrated. The proposed metasurface demonstrates a substantially wider bandwidth for reducing RCS compared to similar works [7, 25–27]. Additionally, the proposed surface achieves a 10 dB RCS reduction bandwidth exceeding 64% for TE and TM polarizations, for large incident angles up to 50 degrees.

2. DESIGN AND ANALYSIS OF THE PRRS

Suggested PRRS unit cell is a combination of a circle and an arrow-shaped structure on FR4 ($h = 1.6$ mm, $\varepsilon_r = 4.3$) as shown in Fig. 1(a). The he dimensions of the structure are as follows: $r = 1.5$ mm, $r_1 = 1.8$ mm, $d = 2.8$ mm, $d_1 = 2.4$ mm, $d_2 = 1.15$ mm, $d_3 = 0.2$ mm, and $P = 6$ mm. Floquet port excitation and unit cell boundary conditions are used to conduct the simulations. In the 'X' and 'Y' directions, we use the unit cell boundary conditions, whereas in $Z_{\max}$ direction Floquet port is employed. The simulated result for y polarized incidence is illustrated in Figs. 1(b) & (c).

Simulated results of r_{yy} (co-polarisation) and r_{yx} (cross-polarisation) reflections versus frequency are represented in Fig. 1(b). It shows that r_{yy} is less than -10 dB in the span of 12.3 to 23.6 GHz. PCR value, as determined by Eq. (1) in the next section, is more than 0.9 as shown in Fig. 1(c). At three different resonance frequencies, 13, 17.7, and 22.8 GHz, the PCR values are very close to 1. It can be concluded that an efficiency of 90% is achieved in the conversion from y-polarized incident wave to X-polarized reflected wave in the frequency band of approximately 12 to 24 GHz. Attributed to the symmetry of the unit cell, outcome remains unaltered for X-polarized incident waves.

2.1. Theoretical Analysis

Consider a regularly incident Y-polarized electromagnetic (EM) wave travelling in 'Z' direction incident on a PRRS. The PCR is defined as [4]:

$$\mathrm{PCR} = \frac{|r_{xy}|^2}{|r_{xy}|^2 + |r_{yy}|^2} \tag{1}$$

$$\text{where} \quad r_{xy} = \frac{\left|\overrightarrow{E_{xr}}\right|}{\left|\overrightarrow{E_{yi}}\right|} \quad \text{and} \quad r_{yy} = \frac{\left|\overrightarrow{E_{yr}}\right|}{\left|\overrightarrow{E_{yi}}\right|} \tag{2}$$

$\overrightarrow{E_{yi}}$ is an incoming wave with a linear y polarisation, $\overrightarrow{E_{yr}}$ and $\overrightarrow{E_{xr}}$ are electric fields that have been reflected with y and x polarisations, respectively. It is possible to separate Y-polarized incident wave as illustrated in Fig. 2. The incident wave may be written as,

$$\vec{E}_i = E_i e^{jkz} Y \tag{3}$$

Equation (3) can be resolved in 'u' and 'v' components as,

$$\vec{E}_i = \sqrt{2}/2 E_i e^{jkz} u + \sqrt{2}/2 E_i e^{jkz} v = E_{iu} + E_{iv} \tag{4}$$

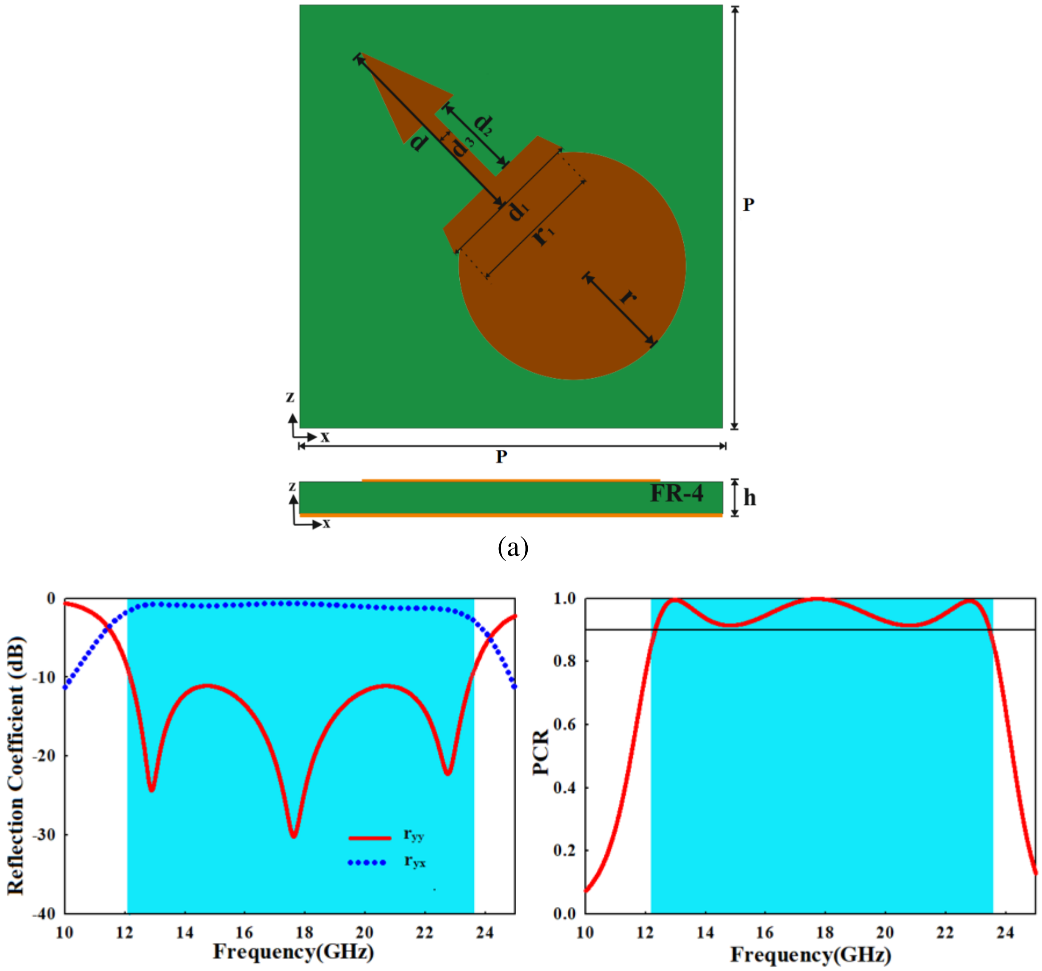

(a)

(b) (c)

Figure 1. (a) Structural geometry ($r = 1.5\,\mathrm{mm}$, $r_1 = 1.8\,\mathrm{mm}$, $d = 2.8\,\mathrm{mm}$, $d_1 = 2.4\,\mathrm{mm}$, $d_2 = 1.15\,\mathrm{mm}$, $d_3 = 0.2\,\mathrm{mm}$, and $P = 6\,\mathrm{mm}$). (b) Simulation results of co(r_{yy}) and cross(r_{yx}) polarisation reflection, (c) PCR under 'Y' polarized incidence.

The reflected field E_r may be stated as,

$$\begin{bmatrix} E_r^u \\ E_r^v \end{bmatrix} = \begin{bmatrix} r_{uu} & r_{uv} \\ r_{vu} & r_{vv} \end{bmatrix} \begin{bmatrix} E_i^u \\ E_i^v \end{bmatrix} \tag{5}$$

$$\begin{aligned} \vec{E}_r &= \sqrt{2}/2\left[r_{uu}E_i e^{j(-kz+\emptyset_{uu})} + r_{uv}E_i e^{j(-kz+\emptyset_{uv})}\right]u + \sqrt{2}/2[r_{vv}E_i e^{j(-kz+\emptyset_{vv})} \\ &\quad + r_{vu}E_i e^{j(-kz+\emptyset_{vu})}]v = \vec{E_{ru}} + \vec{E_{rv}} \end{aligned} \tag{6}$$

where r_{uu}, r_{uv}, r_{vu}, r_{vv} represent co & cross polarized reflection coefficients, and $\emptyset_{uu}$, $\emptyset_{vu}$, $\emptyset_{vu}$, $\emptyset_{vv}$ are the corresponding reflection phases. Amongst r_{uu} and r_{vv} there is a phase difference of $\Delta\emptyset$. Electric field directions across the 'u' & 'v' axes will switch reversely, if $r_{uu} = r_{vv}$ and phase difference, $\Delta\emptyset = \emptyset_{uu} - \emptyset_{vv} = 180^0$. Then resultant of E_{ru} and E_{rv} will be oriented across the x-axis.

Figure 2(a) depicts the incident 'Y' polarized wave, its resolution into the 'u' and 'v' directions (E_{iu} and E_{iv}), and the resultant reflected wave. In Fig. 2(a), the unit cell performs a 90° rotation on the y-polarized incident wave E_i, transforming it into an X-polarized reflected wave. For the mirror image of this unit cell, illustrated in Fig. 2(b), the procedure described above applies, except that E_r is oriented along '$-X$' direction.

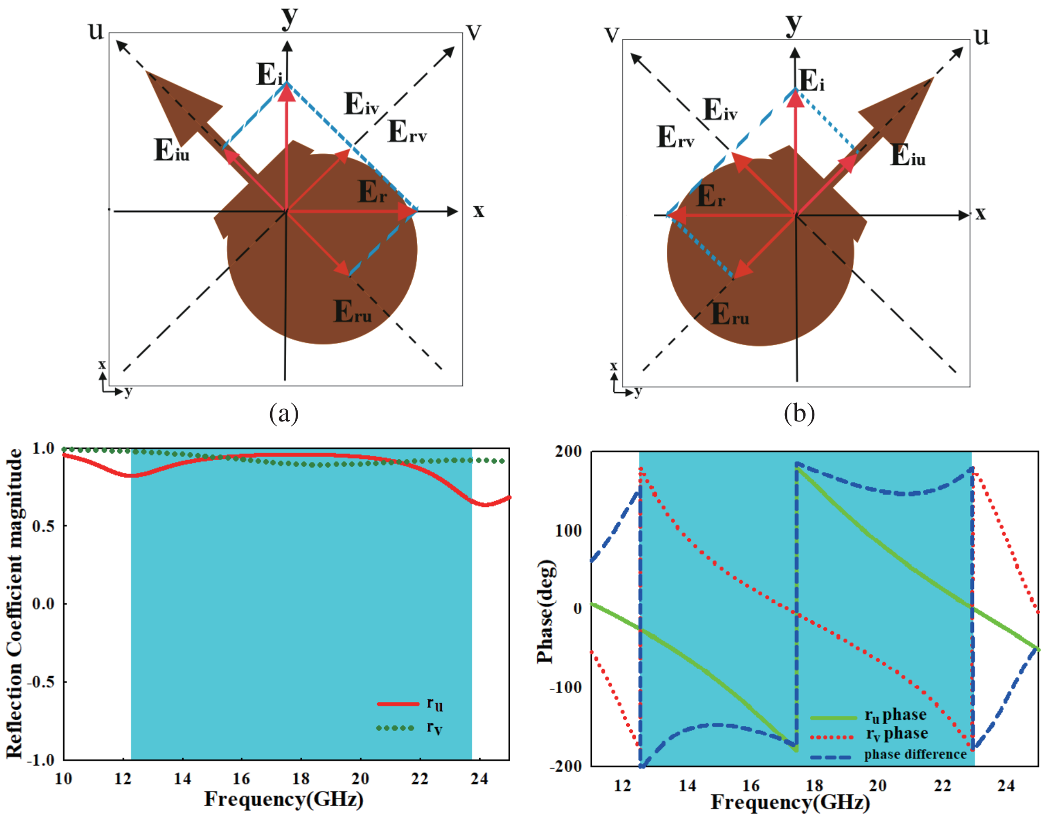

(a) (b)

(c) (d)

Figure 2. Waves resolved into orthogonal components 'u' and 'v' (a) unit cell, (b) mirror of unit cell, (c) reflectance amplitude ($r_u = \frac{E_{ru}}{E_{iu}}$ and $r_v = \frac{E_{rv}}{E_{iv}}$), (d) corresponding phase.

Figures 2(c) & (d) depict reflection amplitude and phase difference with the incident plane electromagnetic wave components across the 'u' and 'v' axes. Both reflection curves have amplitudes proximal to 1, and the phase difference between them is almost 180° in the range 12.3 to 23.6 GHz. This means that significant polarization conversion efficiency has been achieved.

2.2. The Evolution of the Designed Structure

The proposed unit cell undergoes a three-stage evolutionary process to enhance its performance and achieve a broader bandwidth. In the initial stage, a rectangular strip measuring 5.5×3 mm is designed, resulting in a bandwidth of 10–14.5 GHz, as depicted in Fig. 3(a). The length is roughly equal to half

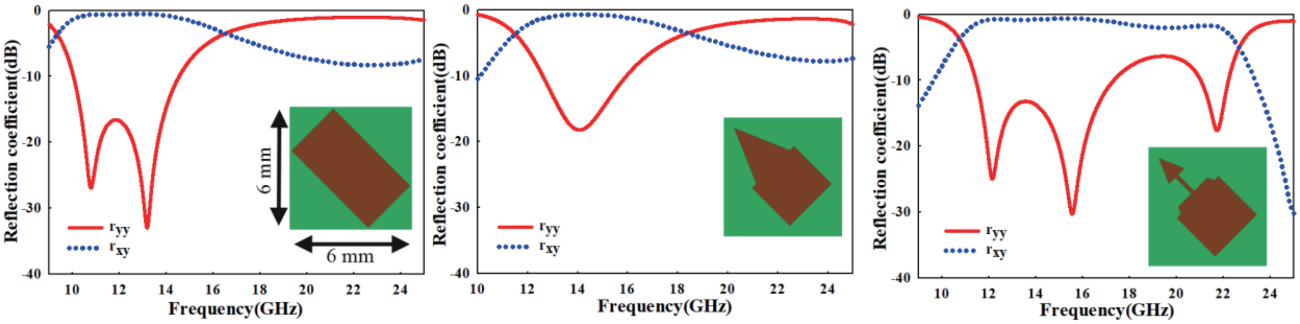

(a) (b) (c)

Figure 3. Simulated results of co & cross polarisation reflections (a) stage 1, (b) stage 2, (c) stage 3.

wavelength in the dielectric ($e = 4.3$, $h = 1.6\,\mathrm{mm}$) for this frequency band. Next, a triangular structure is added to the strip as shown in Fig. 3(b), without changing the overall length. Here again, the unit cell remains a polarization rotator (PR), but the bandwidth achieved is limited to 12.5–15.9 GHz. In the third stage, a trapezoidal section is cut from the triangular structure as depicted in Fig. 3(c). This modification enhances the bandwidth, but with reduced matching across some frequencies. Now, a truncated circle shape is attached to the triangle, replacing the rectangular section at the bottom, which gives a better performance across a broader frequency range. This new configuration, shown in Fig. 1(a), produces notable improvements, as seen in Fig. 1(b). With this design, the unit cell provides an enhanced bandwidth with better matching performance.

2.3. Parameter Optimization

Thorough parameter analysis is conducted to learn more about the impact that the variables shown in Fig. 1(a) have on the reflection rotation properties. Fig. 4(a) illustrates the effect of varying ‘d’ with other variables held constant. As ‘d’ is incremented, the resonant frequency decreases; the bandwidth of the PRRS narrows down; and multi band PR is achieved. The optimum value of ‘d’ is taken as 2.8 mm.

The effect of base length variable ‘d_1’ is studied in Fig. 4(b). It is plain to notice that the base length variation of the triangle does not have much effect on the performance. Figs. 4(c) & (d) show the effect of height of rectangular cut width ‘d_2’ in the triangle and width of the rectangular strip ‘d_3’ attached to the rectangular cut. It is found that the variation of ‘d_2’ has almost zero effect. But the variation of ‘d_3’ causes a reduction in bandwidth, and the optimum value chosen is 0.3 mm. The effect of periodicity is studied and shown in Fig. 4(e). The optimum value of periodicity $P = 6\,\mathrm{mm}$.

Surface current distributions on the structure are studied at three resonating frequencies to deduce the physical mechanism behind this PR. The simulated surface current distributions on upper and lower layers of the metasurface at 13, 17.7, and 22.8 GHz are analysed in Figs. 5(a), (b), & (c).

At 13 & 17.7 GHz, anti-parallel currents are produced on both upper and bottom planes. It indicates the presence of magnetic resonance, which is caused by the formation of current loops in the

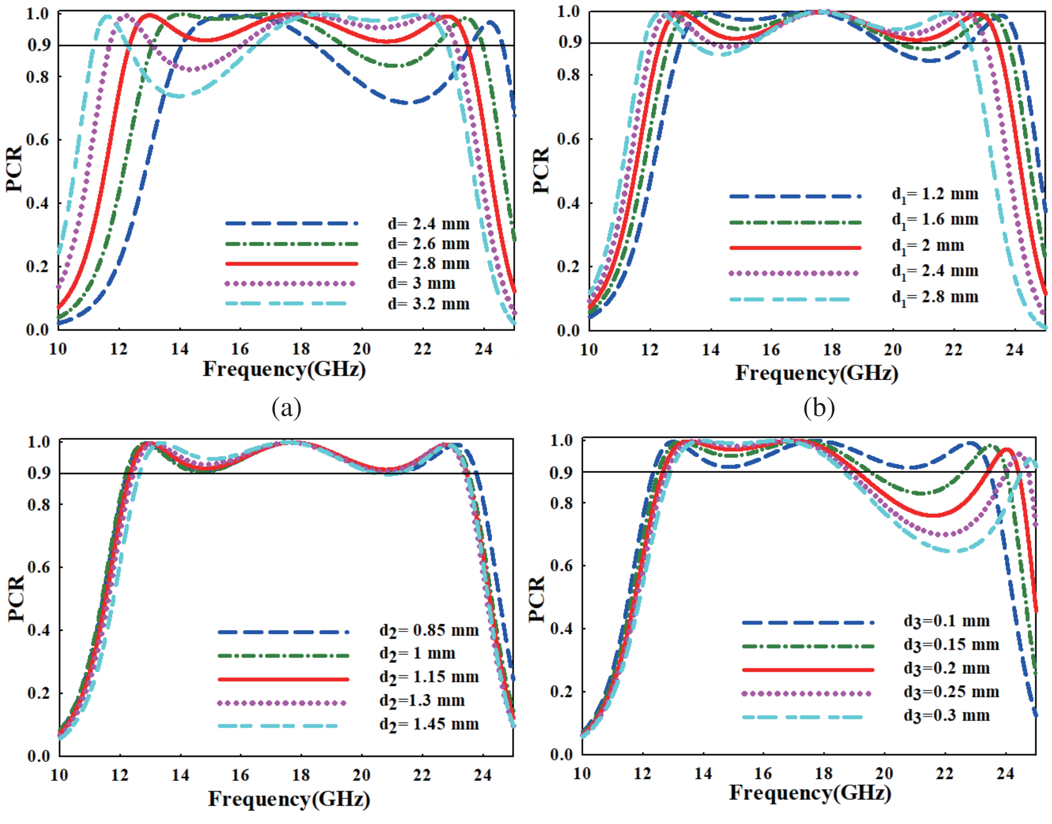

(a) (b)

(c) (d)

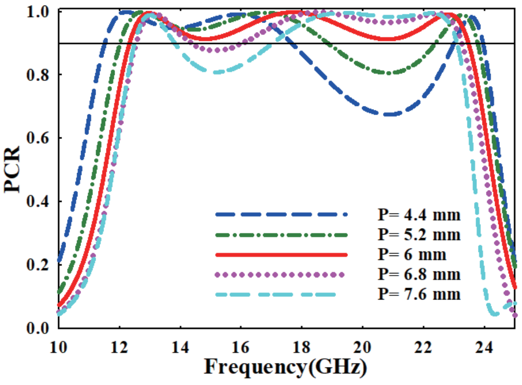

(e)

Figure 4. Parametric study of the PRRS by varying (a) ‘d’, (b) ‘d_1’, (c) ‘d_2’, (d) ‘d_3’ and (e) ‘P’.

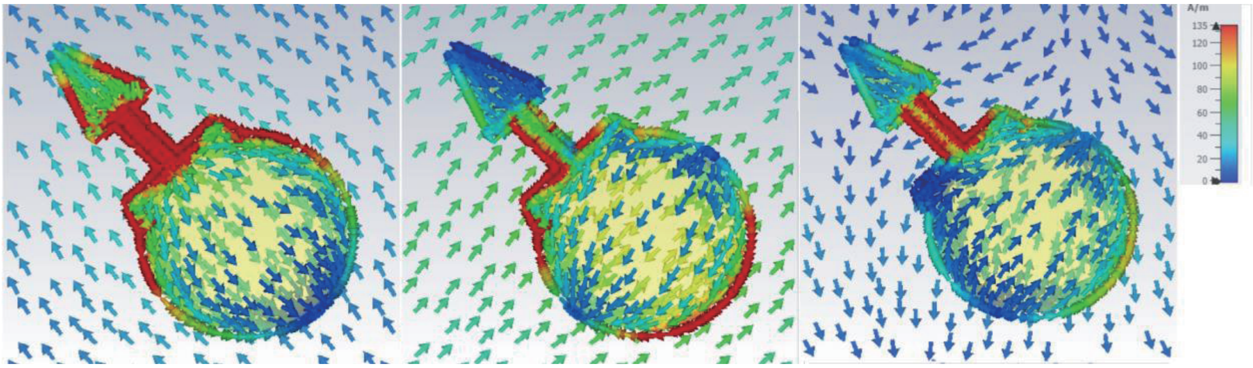

(a) (b) (c)

Figure 5. Surface current distribution in upper and lower layer of suggested structure at various resonating frequencies (a) 13 GHz, (b) 17.75 GHz and (c) 22.86 GHz.

intermediate dielectric layer [28–30]. In contrast, electric resonance occurs around 22.8 GHz when the surface current along the structure is parallel to that on the background sheet. As per the interpretation of results, these magnetic resonances and electric resonance are responsible for the suggested reflecting type polarisation converter’s broadband character.

3. FABRICATION AND MEASUREMENT

In order to test the PRRS, a 10 × 10 array of PRRS unit cells is prototyped on an FR4 substrate. The pattern is etched using the conventional photolithographic process. The structure of the PRRS is depicted in Figs. 6(a) & (b). The graphs of co- and co-polarization reflection and PCR are shown in Figs. 7(a) & (b), which match up well with those of the unit cell. Measurements are done in ‘Ku’ and ‘K’ bands in an anechoic environment using Keysight PNA N5227A network analyser (10–67 GHz) as demonstrated in Figs. 6(c) & (d). The target is placed at a distance of 2 m from the antennas in order to fulfil the far field condition. Also, time gating was utilized to minimise any number of residue reflections. The structure is placed in front of antennas, and the horns are properly aligned to ensure normal incidence. The two antennas can transmit or receive either ‘Y’ or ‘X’ polarized waves.

The measured data of PRRS is normalised by comparing it with PEC surface of the same size. The results for the PRRS array for normal incidence of ‘Y’ polarized EM wave for ‘Ku’ and ‘K’ bands are given in Fig. 7. The measured result shows that the bandwidth of 67% ranging from 12 to 24 GHz is obtained with PCR greater than 90%. The matching between simulated and measured findings is satisfactory in the frequency range with some deviations at a few frequency points. The same result is expected for ‘X’ polarized incidence owing to symmetry of structure.

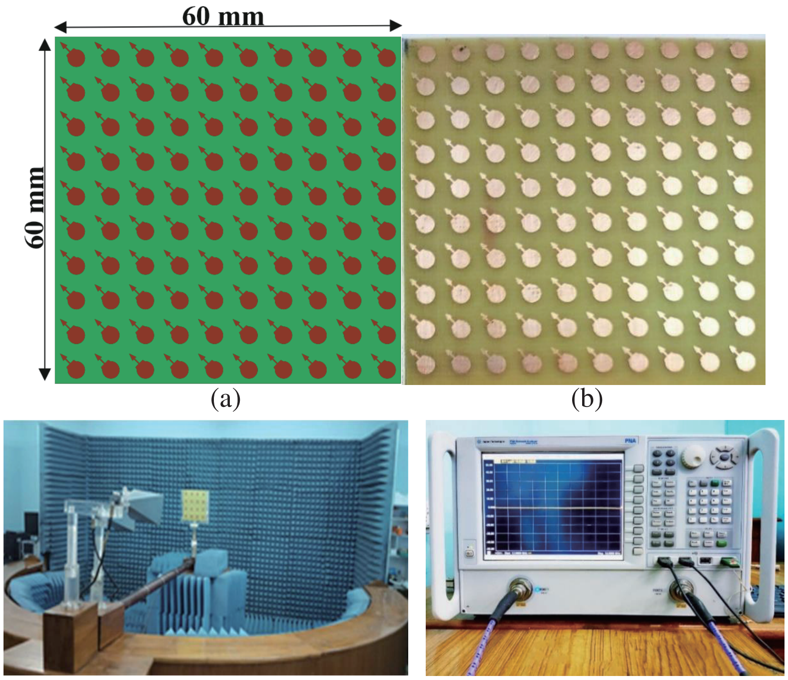

(a) (b)

(c) (d)

Figure 6. (a) PRRS array, (b) fabricated prototype, (c), (d) measurement setup.

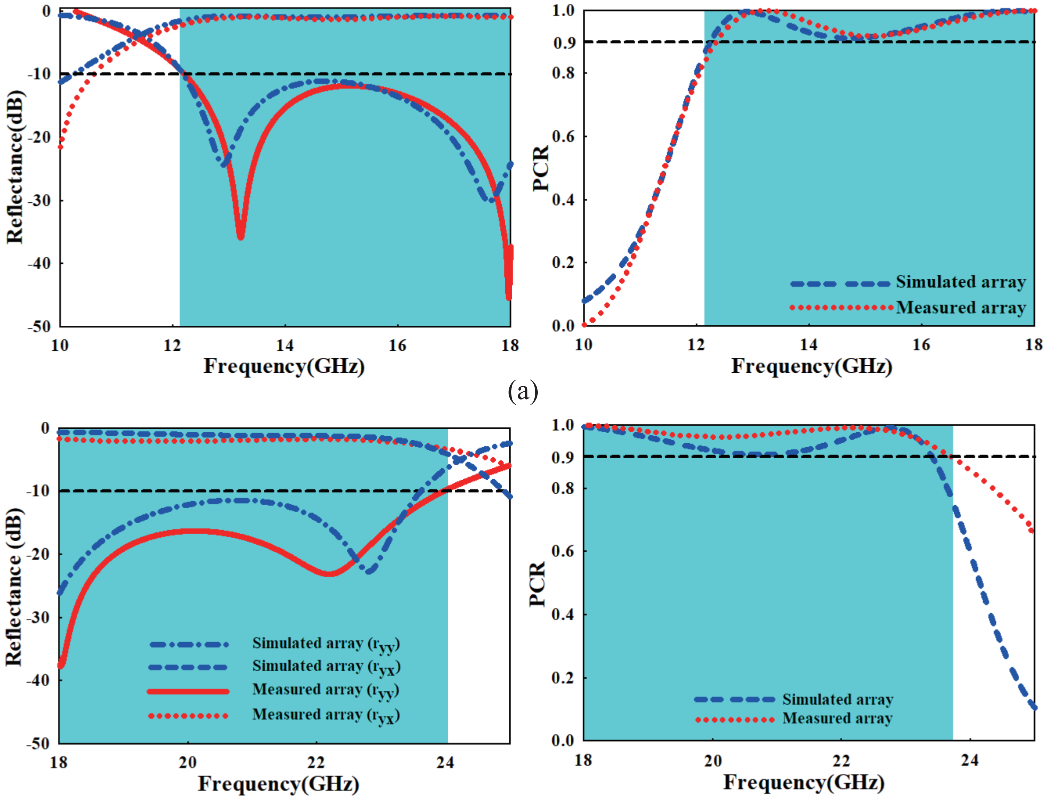

(a)

(b)

Figure 7. Cross- and co-polarization reflection and PCR (a) Ku band, (b) K band.

4. RCS REDUCTION BASED ON PRRS

4.1. Theory, Design and Results

Here the suggested PRRS is applied to RCS reduction. By taking advantage of polarisation conversion characteristics, the metasurface is assembled in a checkerboard configuration as illustrated in Fig. 8. For 'Y' polarized incident wave, the reflected wave is converted to 'X' and '$-X$' polarized ones by orthogonal array elements in the checkerboard as shown in Fig. 8(c). Hence, reflected fields get cancelled resulting in wideband RCS reduction. Due to symmetry, the same result is obtained for X polarized incidence.

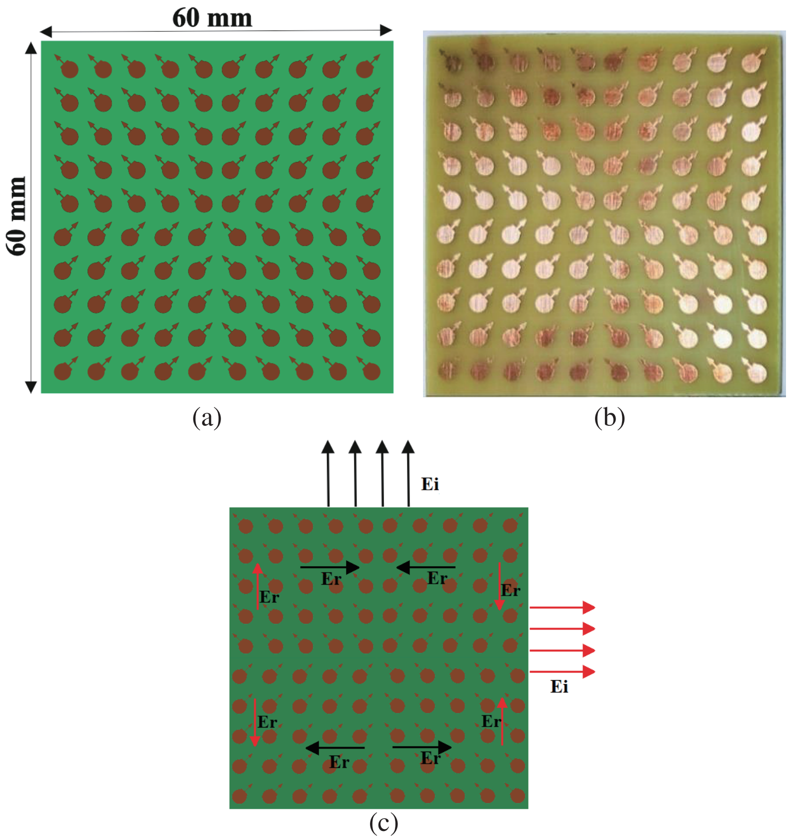

(a) (b)

(c)

Figure 8. (a) Simulated array. (b) Fabricated prototype. (c) Reflection mechanism of the checkerboard.

The RCS reduction of this structure, r_{yy} (dB) in comparison to that of a similar sized PEC surface, may be approximately calculated as follows [31]:

$$r_{yy}(\mathrm{dB}) = 10\log_{10}\left[\frac{\lim\limits_{R\to\infty} 4\pi R^2 \left(\frac{|\overline{E_{ry}}|}{|\overline{E_{iy}}|}\right)^2}{\lim\limits_{R\to\infty} 4\pi R^2 \left(1\right)^2}\right] = 10\log_{10}\left[1-\mathrm{PCR}\right] \tag{7}$$

It is possible to draw the following conclusion from the equation shown above: in order to attain an acceptable RCS reduction across a large frequency range, one must use wideband PRRS that has a high PCR (more than 0.9). As a result, the suggested unit cells are laid out in an orthogonal pattern over four sections to create a checkerboard surface.

A 5 × 5 array of the suggested PCM unit cells and its mirrors are laid out in four sections as depicted in Figs. 8(a) and (b) to verify the proposed hypothesis. RCS reduction of the checkerboard surface for TE and TM incident waves for normal incidence is portrayed in Fig. 9(a). The measured bandwidth ranges from 11.67 to 23.7 GHz. The maximum RCS reduction obtained is 40 dB at 12.7 GHz and 18 GHz. The suggested structure is effective in reducing the RCS for both TE and TM polarized incident waves due to the presence of mirror arrow PCM unit cells along both the '*X*' & '*Y*' axes. Matching between simulated and measured findings is satisfactory in the frequency range with some minor deviations. The fabrication imperfections and measurement uncertainties play an important role in causing this difference. Figs. 9(b) and (c) demonstrate the performance for TE and TM polarized oblique incident waves up to an incidence angle of 60°. As can be shown, the suggested metasurface has a 10 dB RCS reduction of over 66% for TE-polarization and over 64% for TM-polarization at incidence angles up to 50°.

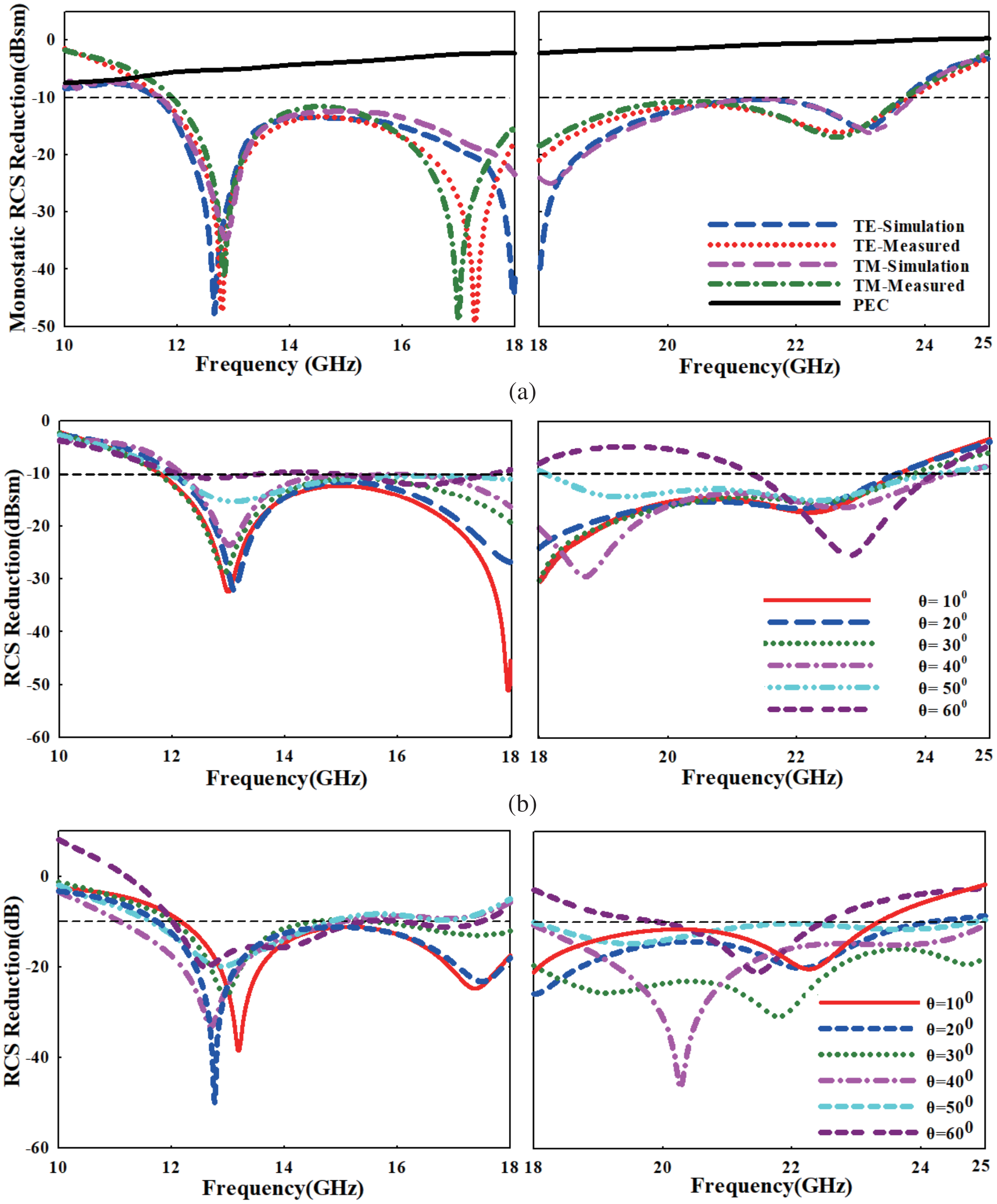

(a)

(b)

(c)

Figure 9. (a) RCS reduction K and ku band for normal incidence, (b) RCS variation with incidence angles for TE waves, (c) for TM waves.

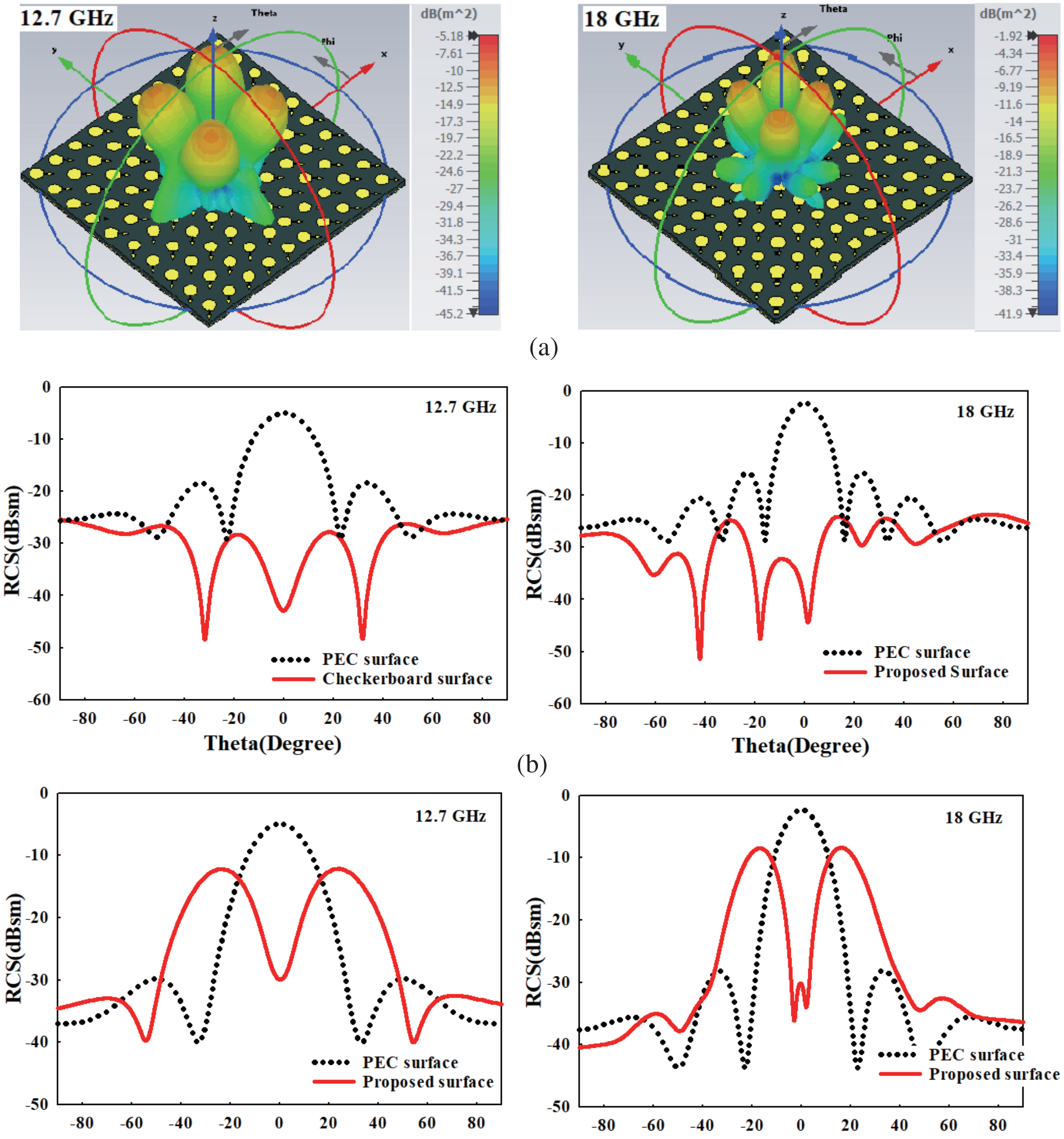

(a)

(b)

(c)

Figure 10. (a) 3D illustration of the RCS pattern of the metasurface, (b) $\phi = 90°$, (c) $\phi = 45°$.

Figure 10(a) depicts the 3D scattered pattern of suggested metasurface at 12.7 and 18 GHz, which corresponds to the dips in RCS decrease vs frequency characteristics shown in Fig. 9(a). These graphs demonstrate how the surface deflects the incident wave and lowers the RCS. The reflecting fields from the surface are split into four at an elevation of $\theta = 20.8°$, one each at $\phi = 45°$, 135°, 225°, and 315°. As illustrated in Figs. 10(b) & (c), the suggested metasurface reduces the RCS at $\phi = 90°$ and $\phi = 45°$ planes over 40 dB and 30 dB at 12.7 GHz and 18 GHz accordingly, in comparison to the maximal RCS at these frequencies.

5. PERFORMANCE-COMPARISON

Table 1 summarises the parameters of the design in comparison to previous works. Our suggested architecture with minimal manufacturing complexity achieves the reported 10 dB RCSR bandwidth of 69% while significantly reducing overall size and thickness, as shown in the table. The suggested

Table 1. Performance compared to other wideband RCS suppressors.

Ref. No.	Method	RCS reduction BW	Electrical size (width × length × thickness)	No. of layers	No. of vias	Fabrication complexity
[23]	EBG	61% (3.94–7.4 GHz) 24% (8.4–10.72 GHz)	$0.18\lambda_0 \times 0.18\lambda_0 \times 0.18\lambda_0$	single	0	Moderate
[20]	AMC	91% (3.75–10 GHz)	$0.18\lambda_0 \times 0.18\lambda_0 \times 0.18\lambda_0$	single	0	Moderate
[21]	AMC	96.7% (8.11–23.32 GHz)	$0.28\lambda_0 \times 0.28\lambda_0 \times 0.05\lambda_0$	Three	0	Moderate
[3]	PRRS	103.6% (5.98–18.84 GHz) PCR = 50%	$0.23\lambda_0 \times 0.23\lambda_0 \times 0.05\lambda_0$	single	2	Moderate
[4]	PRRS	98% (6.1–17.8 GHz)	$0.12\lambda_0 \times 0.12\lambda_0 \times 0.12\lambda_0$	single	4	High
[35]	PRRS	97.69% (4.44–12.92 GHz)	$0.08\lambda_0 \times 0.08\lambda_0 \times 0.08\lambda_0$	Two	4	High
[32]	PRRS	X-polarized 97.50% (5.2–15.0 GHz) y-polarized 112.50% (4.77–17.08 GHz)	$0.15\lambda_0 \times 0.15\lambda_0 \times 0.06\lambda_0$	Three	0	High
[6]	PRRS	97.69% (4.44–12.92 GHz)	$0.08\lambda_0 \times 0.08\lambda_0 \times 0.08\lambda_0$	Two	4	High
[33]	PRRS	126.5% (9–40 GHz)	$0.25\lambda_0 \times 0.25\lambda_0 \times 0.08\lambda_0$	Two	0	High
[25]	PRRS	39% 7.6–11.3 GHz	$0.21\lambda_0 \times 0.21\lambda_0 \times 0.086\lambda_0$	single	0	Low
[36]	PRRS	106.7% (5 dB bandwidth) 6.3–20.7 GHz	$0.21\lambda_0 \times 0.21\lambda_0 \times 0.077\lambda_0$	single	0	Low
[31]	PRRS	103.6% (3 dB bandwidth only) 5.98–18.84 GHz	$0.24\lambda_0 \times 0.24\lambda_0 \times 0.06\lambda_0$	single	0	Low
[34]	PRRS	89.5% (5 dB BW) (8.2 GHz to 21.8 GHz)	$0.19\lambda_0 \times 0.19\lambda_0 \times 0.05\lambda_0$	single	0	Low
[26]	PRRS	9.49% (8.33 GHz–9.16 GHz) 38.16% (12.81 GHz–18.85 GHz)	$0.21\lambda_0 \times 0.21\lambda_0 \times 0.13\lambda_0$	single	0	Low
[27]	PRRS	80% (6–14 GHz)	$0.2\lambda_0 \times 0.2\lambda_0 \times 0.11\lambda_0$	single	0	Low
This study	PRRS	69% (11.6–23.7 GHz) PCR > 90%	$0.240\lambda_0 \times 0.240\lambda_0 \times 0.060\lambda_0$	single	0	Low

surface is constructed on a lightweight, inexpensive FR-4 substrate, which reduces cost and increases its practical utilities.

6. CONCLUSION

A novel PRRS is conceptualised, modelled, and prototyped for wide band RCS reduction. The PRRS unit cell used here has a size of just $0.24\lambda_0 \times 0.24\lambda_0 \times 0.06\lambda_0$ at its lowest operational frequency. The measured result of the proposed design shows more than 90% of PCR in its operating bandwidth. This wideband PRRS was implemented for RCS reduction. This wide-band behaviour is obtained despite the fact that total dimensions and thickness of the structure are lower than those of previous methods. The primary benefits of this design are a high bandwidth, a miniaturized design having less thickness, a lighter weight, and less complicated prototype-fabrication, amongst other benefits. They make it appropriate for practical applications.

ACKNOWLEDGMENT

The authors acknowledge the support from the Centre for Continuing Education, Govt of Kerala and CSIR Emeritus Scientist scheme.

REFERENCES

1. Freialdenhoven, T., T. Bertuch, S. Stanko, D. Nötel, D. I. L. Vorst, and T. Dallmann, "Design of a polarization rotating SIW-based reflector for polarimetric radar application," *IEEE Trans. Antennas Propag.*, Vol. 68, No. 11, 7414–7422, 2020.
2. Nguyen, B., J. Lanteri, J.-Y. Dauvignac, C. Pichot, and C. Migliaccio, "94 GHz folded Fresnel reflector using C-patch elements," *IEEE Trans. Antennas Propag.*, Vol. 56, No. 11, 3373–3381, 2008.
3. Jia, Y., Y. Liu, Y. J. Guo, K. Li, and S.-X. Gong, "Broadband polarization rotation reflective surfaces and their applications to RCS reduction," *IEEE Trans. Antennas Propag.*, Vol. 64, No. 1, 179–188, 2015.
4. Jia, Y., Y. Liu, Y. J. Guo, K. Li, and S. Gong, "A dual-patch polarization rotation reflective surface and its application to ultra-wideband RCS reduction," *IEEE Trans. Antennas Propag.*, Vol. 65, No. 6, 3291–3295, 2017.
5. Zheng, Q., C. Guo, H. Li, and J. Ding, "Broadband radar cross-section reduction using polarization conversion metasurface," *International Journal of Microwave and Wireless Technologies*, Vol. 10, 197–206, January 2018.
6. Fang, W., D. G. Fan, X., Y. Xie, X. C. Liu, S. N. Sun, and P. Chen, "A broadband radar cross section reduction metasurface based on polarization conversion and scattering cancellation," *IEEE Xplore*, Vol. 15, August 2019.
7. Yin, J. Y., H. J. Sun, and L. Zhang, "An ultra-wideband polarization conversion metasurface and its application in RCS reduction," *Progress In Electromagnetics Research Letters*, Vol. 89, 29–36, 2020.
8. Jeyaraj, J. P. G. and A. Swaminathan, "Broadband RCS reduction in microstrip patch antenna using L-shape stepped polarization rotation reflective surface," *Int. J. RF Microw. Comput. Aided Eng.*, Vol. 28, 2018.
9. Liu, Y., K. Li, Y. Jia, Y. Hao, S. Gong, and Y. J. Guo, "Wideband RCS reduction of a slot array antenna using polarization conversion metasurfaces," *International Journal of Antennas and Propagation*, Vol. 64, 326–331, 2016.
10. Gao, X., X. Han, W.-P. Cao, H. O. Li, H. F. Ma, and T. J. Cui, "Ultrawideband and high-efficiency linear polarization converter based on double V-shaped metasurface," *IEEE Trans. Antennas Propag.*, Vol. 63, 3522–3530, 2015.
11. Lin, B. Q., X. Y. Da, J. L. Wu, W. Li, Y. W. Fang, and Z. H. Zhu, "Ultra-wideband and high-efficiency cross polarization converter based on anisotropic metasurface," *Microw. Opt. Technol. Lett.*, Vol. 58, 2402–2405, 2016.
12. Moghadam, M. S. J., M. Akbari, F. Samadi, and A.-R. Sebak, "Wideband cross polarization rotation based on reflective anisotropic surfaces," *IEEE Access*, Vol. 6, 15919–15925, 2018.
13. Guo, L., S. Li, X. Jiang, et al., "Ultra-wideband polarization rotation reflective metasurface based on monolayer rhombus hollow structure," *AIP Advances*, Vol. 8, 095205, 2018.
14. Grady, N. K., J. E. Heyes, D. R. Chowdhury, Y. Zeng, M. T. Reiten, A. K. Azad, A. J. Taylor, D. A. R. Dalvit, and H.-T. Chen, "Terahertz metamaterials for linear polarization conversion and anomalous refraction," *Science*, Vol. 340, No. 6138, 1304–1307, 2013.
15. Zhao, J., N. Li, and Y. Cheng, "All-dielectric InSb metasurface for broadband and high-efficient thermal tunable terahertz reflective linear-polarization conversion," *Optics Communications*, Vol. 536, 129372, 2023.
16. Jiang, H., J. Wang, S. Zhao, L. H. Ye, H. Zhang, and W. Zhao, "Active optical switch and polarization-selective absorption in a VO_2 based metasurface in THz region," *Optics Communications*, Vol. 536, 129380, 2023.
17. Cheng, Y., D. Yang, and X. Li, "Broadband reflective dual-functional polarization convertor based on all-metal metasurface in visible region," *Physica B*, Vol. 640, 414047, 2022.
18. Yang, D., Y. Cheng, F. Chen, H. Luo, and L. Wu, "Efficiency tunable broadband terahertz graphene metasurface for circular polarization anomalous reflection and plane focusing effect," *Diamond &*

Related Materials, Vol. 131, 109605, 2023.

19. Sorathiyal, V., S. Lavadiya1, B. Parmar, S. Das, M. Krishna, O. S. Faragallah, M. Baz, M. M. A. Eid, and A. N. Z. Rashed, "Numerical investigation of the tunable polarizer using gold array and graphene metamaterial structure for an infrared frequency range," *Applied Physics B*, Vol. 128, 2022.
20. Modi, A. Y., C. A. Balanis, C. R. Birtcher, and H. N. Shaman, "Novel design of ultra-broadband radar cross section reduction surfaces using artificial magnetic conductors," *IEEE Trans. Antennas Propag.*, Vol. 65, No. 10, 5406–5417, 2017.
21. Zaker, R. and A. Sadeghzadeh, "Wideband radar cross section reduction using a novel design of artificial magnetic conductor structure with a triple layer chessboard configuration," *Int. J. RF Microw. Comput.-Aided Eng.*, Vol. 29, No. 2, 2019.
22. Xue, J., W. Jiang, and S. Gong, "Chessboard AMC surface based on quasi-fractal structure for wideband RCS reduction," *IEEE Antennas and Wireless Propagation Letters*, Vol. 17, No. 2, 201–204, 2018.
23. Chen, W., C. A. Balanis, and C. R. Birtcher, "Dual wide-band checkerboard surfaces for radar cross section reduction," *IEEE Trans. Antennas Propag.*, Vol. 64, No. 9, 4133–4138, 2016.
24. Ghayekhloo, A., M. Afsahi, and A. A. Orouji, "An optimized checkerboard structure for cross-section reduction: Producing a coating surface for bistatic radar using the equivalent electric circuit model," *IEEE Antennas Propag. Mag.*, Vol. 60, No. 5, 78–85, 2018.
25. Khalaj-Amirhosseini, M. and M. Khanjarian, "Radar cross section reduction using polarization cancellation approach," *Progress In Electromagnetics Research Letters*, Vol. 74, 107–110, 2018.
26. Patel, K. and M. Joshi, "Broadband radar cross section reduction of microstrip antenna using polarization conversion metasurface," *Progress In Electromagnetics Research B*, Vol. 96, 67–86, 2022.
27. Yang, J. J., Y. Z. Cheng, C. C. Ge, and R. Z. Gong, "Broadband polarization conversion metasurface based on metal cut-wire structure for radar cross section reduction," *Materials*, Vol. 11, 2018.
28. Mei, Z. L., X. M. Ma, C. Lu, and Y. D. Zhao, "High-efficiency and wide bandwidth linear polarization converter based on double U-shaped metasurface," *AIP Adv.*, Vol. 7, 125323, 2017.
29. Xu, J., R. Li, J. Qin, S. Wang, and T. Han, "Ultra-broadband wide-angle linear polarization converter based on H-shaped metasurface," *Optics Express*, Vol. 26, No. 16, 20913, 2018.
30. Kamal, B., J. Chen, Y. Yingzeng, J. Ren, S. Ullah, and W. U. R. Khan, "High efficiency and ultra-wideband polarization converter based on an L-shaped metasurface," *Opt. Mater. Express*, Vol. 11, 1343–1352, 2021.
31. Jia, Y., Y. Liu, Y. J. Guo, K. Li, and S. Gong, "Broadband polarization rotation reflective surfaces and their application to RCS reduction," *IEEE Trans. Antennas Propag.*, Vol. 64, No. 1, 179–188, 2016.
32. Li, S. J., X. Y. Cao, L. M. Xu, et al., "Ultra-broadband reflective metamaterial with RCS reduction based on polarization convertor, information entropy theory and genetic optimization algorithm," *Sci. Rep.*, Vol. 6, No. 37409, 2016.
33. Ameri, E., S. H. Esmaeli, and S. H. Sedighy, "Ultra wideband radar cross section reduction by using polarization conversion metasurfaces," *Scientific Reports*, No. 478, 2019.
34. Mu, X., M. Lv, and T. Ni, "Design of an ultra-broadband polarization rotating reflective surface for the reduction of radar cross section," *Progress In Electromagnetics Research M*, Vol. 114, 69–78, 2022.
35. Jeyaraj, J. P. G. and A. Swaminathan, "An efficient reflective polarization rotation meta surface for broadband RCS reduction," *International Journal of RF and Microwave Computer-Aided Engineering*, Vol. 28, No. 7, 2018.
36. Chen, W. K., J. F. Shi, Z. Y. Niu, et al., "Broadband polarization conversion metasurface for radar cross section reduction," *ICMMT*, 2018.